Pergamon

Int. J. Heat Mass Transfer. Vol. 39, No. 3, pp. 603–613, 1996
Elsevier Science Ltd
Printed in Great Britain
0017-9310/96 $9.50+0.00

0017-9310(95)00144-1

Investigation of three-dimensional thermocapillary convection in a cubic container by a multi-grid method

V. SAß, H. C. KUHLMANN† and H. J. RATH

Center of Applied Space Technology and Microgravity, ZARM, University of Bremen, 28359 Bremen, Germany

(*Received* 12 *October* 1993 *and in final form* 26 *January* 1995)

Abstract—Three-dimensional thermocapillary convection of a Boussinesq fluid in an open cubic container is considered in the absence of buoyancy. The steady motion is computed with a modified Full-Approximation Scheme, Full Multi-Grid (FAS–FMG) method based on a finite difference, primitive variable formulation. Solutions on a staggered grid of $32 \times 32 \times 32$ points for each unknown are obtained by a line coupled, block implicit relaxation method for the Navier–Stokes equation, and an alternating zebra-relaxation method for the energy equation. Three-dimensional (3D) flow structures and temperature fields are presented for Reynolds numbers up to 5×10^4 and Prandtl numbers $Pr = 0.01$, 1, 10 and 50. Apart from the main vortex known from 2D calculations pronounced secondary vortices appear. The mechanisms driving this secondary flow are discussed in terms of well-known properties of the main vortex.

1. INTRODUCTION

Thermocapillary convection can be an important natural transport mechanism in hydrodynamic systems that involve at least two immiscible fluids. If surface tension variations arise due to, e.g. temperature gradients along the interface (thermocapillary effect), then shear stresses acting on the interface induce fluid motions on either side of the boundary. Because of the relatively low viscosity of gases, the gas flow in liquid–gas systems can be neglected and the interface is considered a thermocapillary free surface. For most liquid–gas systems $d\sigma_0/dT < 0$ and the thermocapillary surface force (and usually also the flow) is directed from hot to cold areas of the liquid. Examples are the melt motion in a weld bath [1] or the flow in the Czochralski crystal-growth process [2]. Under terrestrial gravity conditions thermocapillary convection is generally dominated by buoyant convection. Since the ratio between thermocapillary forces and buoyancy forces scales like d^{-2}, where d is the characteristic length over which the surface tension varies, buoyancy effects play a minor role in small size systems with aspect ratios of order O(1). Carpenter and Homsy [3], however, have shown that thermocapillary convection will also be dominant in even larger systems, if the temperature gradient is sufficiently increased.

For that reason it is interesting to study thermocapillary convection both as a basic surface force driven flow system and for its practical importance. Because of the simple geometry the flow in open cavities, in which the free surface is assumed to be non-deformable, has received much attention during the past years. Graziani *et al.* [4] developed a 2D stationary code for small thermocapillary Reynolds numbers ($Re < 200$). This code was improved by Strani *et al.* [5], who simulated flows up to $Re = 3000$. Both methods used a stream function formulation. Zebib *et al.* [6] introduced a stationary 2D finite difference method in primitive variable formulation. For $Pr = 1$ this method is convergent for Reynolds numbers up to 10^4. In a following paper, Carpenter and Homsy [3] simulated the flow up to Reynolds numbers of 1.9×10^5 using a combination of Newton and chord steps for the iterative solution of the problem. Moreover, the dependence of the convection structure on the Prandtl number was examined and the analogy to the lid driven cavity flow [7] was discussed. Three-dimensional calculations have been reported by Babu and Korpela [8] and Hsieh [9]. Babu and Korpela's calculations were limited to small Reynolds numbers up to $Re = 300$. They demonstrated the existence of secondary flows, which were induced by surface temperature gradients perpendicular to the main temperature gradient applied externally. Hsieh [9] computed the flow for $Pr = 100$ and $Re \cong 400$ by a dual-time stepping method for a deformable surface. The surface deformation was shown to be less than 0.01% of the container linear dimension.

In the present study we investigate steady 3D thermocapillary convection without buoyant convection in a cube and pay special attention to those 3D effects that are induced by the presence of sidewalls.

† Author to whom correspondence should be addressed.

NOMENCLATURE

$Ca = \gamma T_0/\sigma_0$ capillary number
d distance between the heated walls
h, H distance between grid points on the fine/coarse grid
L_1, F_1 difference operator and boundary values refering to the N–S-system
L_2, F_2 difference operator and boundary values refering to the energy equation
$Ma = Pr\,Re$ Marangoni number
p pressure
$Pr = \nu/\kappa$ Prandtl number
$Re = d\gamma T_0/\mu\nu$ Reynolds number
T temperature
T_R boundary values of T on the free surface
T_0 temperature difference between the heated walls
$\mathbf{U} = (u, v, w)^T$ velocity vector.

Greek symbols
$\gamma = d\sigma_0/dT$ surface tension coefficient
κ thermal diffusivity
μ dynamic viscosity
ν kinematic viscosity
σ surface tension
σ_0 surface tension at the reference temperature
Ω bounded domain
Ω_L bounded discrete domain.

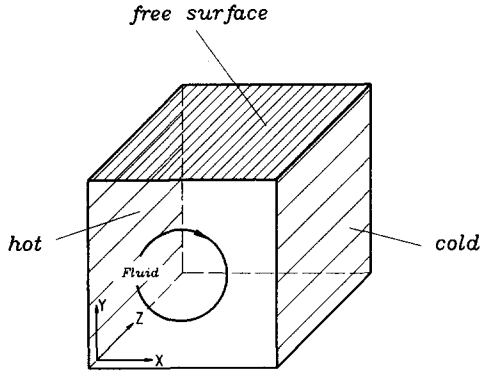

Fig. 1. Cubic cavity with open top and heated walls (hatched) and coordinate system.

2. MATHEMATICAL MODEL

We consider an open-top cubic box shown in Fig. 1 of side length d containing a Boussinesq liquid. The side walls of the box at $x = 0, d$ are kept at constant temperatures of $T = \pm T_0/2$ relative to an arbitrary reference temperature. In non-dimensional form the stationary flow is governed by the Navier–Stokes equations (1,2) and the energy equation (3) inside the domain $\Omega = (0, 1) \times (0, 1) \times (0, 1)$

$$Re(\mathbf{U}\cdot\nabla)\mathbf{U} = -\nabla p + \Delta\mathbf{U} \tag{1}$$

$$\nabla\cdot\mathbf{U} = 0 \tag{2}$$

$$Ma(\mathbf{U}\cdot\nabla)T = \Delta T. \tag{3}$$

Length, velocity, temperature and pressure have been made dimensionless by the scales d, $\gamma T_0/\mu$, T_0 and $\gamma T_0/d$, respectively. The Reynolds and the associated Marangoni number are defined as

$$Re = \frac{d\gamma T_0}{\mu\nu} \quad \text{and} \quad Ma = PrRe$$

with Prandtl number $Pr = \nu/\kappa$. The problem is completed by appropriate boundary conditions. At the rigid walls no-slip and no-penetration boundary conditions are imposed for the velocity $\mathbf{U} = (u, v, w)$,

$$u = v = w = 0 \quad \text{on} \quad x = 0, 1$$

$$u = v = w = 0 \quad \text{on} \quad y = 0$$

$$u = v = w = 0 \quad \text{on} \quad z = 0, 1. \tag{4}$$

In the limit of vanishing capillary number $Ca = \gamma T_0/\sigma_0 \to 0$ surface deformations cannot occur (Ca is usually small in experiments, see Hsieh [9] or Kamotani *et al.* [10]), so that the kinematic condition at the free surface is

$$v = 0 \quad \text{on} \quad y = 1. \tag{5}$$

The balance of forces on the free surface shows that the shear stresses must be compensated by thermocapillary forces. For $Ca = 0$ the boundary conditions are simplified to

$$\frac{\partial u}{\partial y} = -\frac{\partial T}{\partial x} \quad \text{on} \quad y = 1 \tag{6}$$

$$\frac{\partial w}{\partial y} = -\frac{\partial T}{\partial z} \quad \text{on} \quad y = 1. \tag{7}$$

Since the side walls of the box at $x = 0, 1$ are heated and all other walls are considered adiabatic, we impose

$$T = 1 \quad \text{on} \quad x = 0 \tag{8}$$

$$T = 0 \quad \text{on} \quad x = 1 \tag{9}$$

and

$$\frac{\partial T}{\partial y} = 0 \quad \text{on} \quad y = 0, 1 \tag{10}$$

$$\frac{\partial T}{\partial z} = 0 \quad \text{on} \quad z = 0, 1. \tag{11}$$

Note, that no heat transfer is allowed between the liquid and the gas at $y = 1$ [equation (10)].

3. NUMERICAL METHOD

To solve the problem formulated in the previous section we employ a Multi-Grid method. During the course of the computation, the solution is approximated on grids with different mesh sizes. This procedure involves interpolations of the field variables between different grids and relaxations on each grid. We follow Bruneau and Jouron [11] in solving this problem by using a simplification of the FAS–FMG algorithm, which essentially consists of doing a fixed number NBUP = 2 of fine grid iterations, NBDOWN = 1 of coarse grid iterations, and NB1 = 5 iterations on the coarsest grid (we use the same notation as [11]).

One complete iteration cycle is split in two parts. In a first step, **U** and p are calculated. To solve the corresponding equations the temperature distribution entering in the boundary conditions (6, 7) as well as $\mathbf{U}\cdot\nabla$ are approximated by values obtained in the previous iteration step. The linearization of the nonlinear term is sometimes called the *method of frozen-coefficients*. Having determined **U** and p in this manner, the energy equation can be solved without difficulties.

The energy equation is relaxated after the relaxation of the NS equations (1) and (2). The discrete versions of (1)–(3) at the nth iteration can be written as

$$\text{1. step:} \quad L_1(\mathbf{U}^{(n)}, p^{(n)}, \mathbf{U}^{(n-1)}, p^{(n-1)}, T_R^{(n-1)}) = F_1 \tag{12}$$

$$\text{2. step:} \quad L_2(\mathbf{U}^{(n)}, T^{(n)}, T^{(n-1)}) = F_2 \tag{13}$$

where L_i denotes the finite difference operators and F_i denotes the boundary values (except for T_R) for the NS equations ($i = 1$) and the energy equation ($i = 2$). T_R is the temperature distribution on the thermocapillary surface at $y = 1$.

The iterations are carried out on a staggered grid [12] with the pressure p given at the center (i,j,k) of a unit cell, the velocity components $u(i\pm 1/2, j, k)$, $v(i, j\pm 1/2, k)$, $w(i, j, k\pm 1/2)$, and the temperature $T(i\pm 1/2, j, k\pm 1/2)$. The velocities and the pressure in the unit cell are calculated simultaneously. We use a line-implicit method allowing us to calculate pressure gradients in line-direction implicitely. If, e.g. the line relaxation takes place in x-direction, then the following typical system of equations is obtained

$$\begin{bmatrix} A_{u_1} & & & & & & \frac{1}{\Delta x} \\ & A_{u_2} & & & 0 & & -\frac{1}{\Delta x} \\ & & A_{v_1} & & & & \frac{1}{\Delta y} \\ & & & A_{v_2} & & & -\frac{1}{\Delta y} \\ & & & & A_{w_1} & & \frac{1}{\Delta z} \\ & 0 & & & & A_{w_2} & -\frac{1}{\Delta z} \\ & & & & & & A_1 \end{bmatrix} \begin{bmatrix} u_1^{(n)} \\ u_2^{(n)} \\ v_1^{(n)} \\ v_2^{(n)} \\ w_1^{(n)} \\ w_2^{(n)} \\ p^{(n)} \end{bmatrix}$$

$$+ \begin{bmatrix} -\frac{1}{\Delta x} p^{(n)}_{i-1,j,k} \\ \frac{1}{\Delta x} p^{(n)}_{i+1,j,k} \\ 0 \\ 0 \\ 0 \\ 0 \\ A_2 p^{(n)}_{i+1,j,k} \end{bmatrix} + \begin{bmatrix} 0 \\ 0 \\ -\frac{1}{\Delta y} p^{(n-1)}_{i,j-1,k} \\ \frac{1}{\Delta y} p^{(n-1)}_{i,j+1,k} \\ -\frac{1}{\Delta z} p^{(n-1)}_{i,j,k-1} \\ \frac{1}{\Delta z} p^{(n-1)}_{i,j,k+1} \\ 0 \end{bmatrix} + \begin{bmatrix} B_{u_1} \\ B_{u_2} \\ B_{v_1} \\ B_{v_2} \\ B_{w_1} \\ B_{w_2} \\ B \end{bmatrix} = 0 \tag{14}$$

with

$$A_1 = ((\Delta x)^2 A_{u_1})^{-1} + ((\Delta x)^2 A_{u_2})^{-1} + ((\Delta y)^2 A_{v_1})^{-1} + ((\Delta y)^2 A_{v_2})^{-1} + ((\Delta z)^2 A_{w_1})^{-1} + ((\Delta z)^2 A_{w_2})^{-1}$$

$$A_2 = -((\Delta x)^2 A_{u_2})^{-1}$$

$$B = \frac{B_{u_1}}{\Delta x A_{u_1}} - \frac{B_{u_2}}{\Delta x A_{u_2}} + \frac{B_{v_1}}{\Delta y A_{v_1}} - \frac{B_{v_2}}{\Delta y A_{v_2}} + \frac{B_{w_1}}{\Delta z A_{w_1}} - \frac{B_{w_2}}{\Delta z A_{w_2}}.$$

For the calculation of the line-relaxation in x-direction a linear system of equations $Au = b$ made up of submatrices like (14) has to be solved. If the solution vector is arranged linewise, then u_1 and u_2 lie on the same point and we can get the vector of unknowns in the form $(\ldots, u^i, v_1^i, v_2^i, w_1^i, w_2^i, p^i, u^{i+1}, v_1^{i+1}, v_2^{i+1}, w_1^{i+1}, w_2^{i+1}, p^{i+1}, u^{i+2}, \ldots)$. In this case, A is an upper triangular matrix and the system can be solved uniquely if $\operatorname{tr} A \neq 0$. Because of the form of A this requires

$$A_{u_i}, A_{v_i}, A_{w_i}, A_1 \neq 0 \quad \text{for } i = 1, 2. \tag{15}$$

In particular, the condition for A_1 is satisfied if

$$\text{sign}\,(A_{u_i}) = \text{sign}\,(A_{v_i}) = \text{sign}\,(A_{w_i}). \tag{16}$$

The line-relaxation is carried out in alternating zebra-relaxation order, i.e. for constant z the lines with j even are calculated before those with j odd. A complete relaxation step on Ω_L for the N–S-system consists of three single zebra relaxation steps for the three coordinate directions. The relaxation in direction of the y- and the z-axis is carried out in a similar way as for the x-direction described above.

A similar alternating zebra-relaxation method is used for the energy equation. The structure of the relaxation step is identical for the three spacial directions. The linearized difference equation for the energy equation has the form

$$A_{-1} T_{-1}^{(n)} + A_0 T_0^{(n)} + A_{+1} T_{+1}^{(n)} + \sum_k A_k T_k^{(n-1)} = 0$$

with

$$A_i = g(T^{(n-1)}, \mathbf{U}^{(n)}) \tag{17}$$

where the subscripts -1, 0, 1 denote grid points in relaxation direction and k defines all other points involved in the difference scheme. Collecting all difference equations in the line-relaxation interval a linear tridiagonal system (with main diagonal elements A_0 and subdiagonal elements A_{-1} and A_{+1}) is obtained, which is solved by a double-sweep method, see [12]. The tridiagonal system has a unique solution, if the corresponding matrix is strongly diagonal dominant, i.e. if

$$|A_0| > |A_{-1}| + |A_{+1}| \tag{18}$$

for each main diagonal element A_0. Here the condition is guaranteed by appropriate weighting of the convective and diffusive terms. To get a convergent iteration method the unknowns $\mathbf{U}$ and T are updated by under-relaxation after each line-by-line relaxation, the optimum values for the under-relaxation parameters are found to decrease linearly from 1 to 0.1 for increasing Reynolds and Marangoni number from 100 up to 50 000.

For the discretization of the momentum and energy equation we use a scheme based on that of Spalding [13] and which has been used in a similar form by Vanka [12], Thomson and Ferzinger [14] and Bruneau and Jouron [11]. The diffusion term in the momentum equations of (1) is approximated using the well-known three-point formula to get the discretization for

$$u(\partial u/\partial x) - Re^{-1}\partial^2 u/\partial x^2 \quad \text{in} \quad (x + h/2)$$

if $\left| u\left(x+\frac{h}{2}\right)^{(n-1)} \right| < \frac{2}{Re\,h}$

$$u\left(x+\frac{h}{2}\right)^{(n-1)} \frac{u\left(x+\frac{3h}{2}\right)^{(n-1)} - u\left(x-\frac{h}{2}\right)^{(n-1)}}{2h} - \frac{u\left(x-\frac{h}{2}\right)^{(n-1)} - 2u\left(x+\frac{h}{2}\right)^{(n)} + u\left(x+\frac{3h}{2}\right)^{(n-1)}}{Re\,h^2}$$

else, if $u\left(x+\frac{h}{2}\right)^{(n-1)} < 0$

$$u\left(x+\frac{h}{2}\right)^{(n-1)} \times \frac{4u\left(x+\frac{h}{2}\right)^{(n)} - 5u\left(x+\frac{3h}{2}\right)^{(n-1)} + u\left(x+\frac{5h}{2}\right)^{(n-1)}}{3h} - (1+r) \times \frac{u\left(x-\frac{h}{2}\right)^{(n-1)} - 2u\left(x+\frac{h}{2}\right)^{(n-1)} + u\left(x+\frac{3h}{2}\right)^{(n-1)}}{Re\,h^2}$$

else

$$u\left(x+\frac{h}{2}\right)^{(n-1)} \times \frac{-4u\left(x+\frac{h}{2}\right)^{(n)} + 5u\left(x-\frac{h}{2}\right)^{(n-1)} - u\left(x-\frac{3h}{2}\right)^{(n-1)}}{3h} - (1-r) \times \frac{u\left(x-\frac{h}{2}\right)^{(n-1)} - 2u\left(x+\frac{h}{2}\right)^{(n-1)} + u\left(x+\frac{3h}{2}\right)^{(n-1)}}{Re\,h^2} \tag{19}$$

with

$$r = \tfrac{1}{2} Re\, h\, u\left(x+\frac{h}{2}\right)^{(n-1)}.$$

The difference scheme for the other convection and diffusion terms of the N–S equation and the energy equation are similar. It turns out that in both difference equations the coefficients (15) are always positive. Therefore, all main diagonal elements in (14) are positive, so that according to (16) a unique solution of the system exists.

Near the boundaries the discretizations must be modified. If the three-point stencil for the approximation of a convective term crosses the boundary, it

is replaced by the well-known first-order forward or backward difference schemes.

4. RESULTS

4.1. *Code validation*

In order to test our numerical code we first calculated the 2D thermocapillary flow, i.e. the flow in the absence of sidewalls. The calculations have been done for unit aspect ratio (height/width of the cavity) and various values of Re and Ma. For a typical MG run we have used equidistant grids of 32×32, 64×64, 128×128 and 256×256 grid points (level 4 to level 1). The flow and temperature field can be resolved by the 32×32 grid up to 2% of the fully converged solution, except for the position and the magnitude of the peak of the surface velocity u, which is a result of the large temperature gradient near the cold boundary at large Reynolds number.

Highly accurate solutions of this problem have been given by Zebib *et al.* [6] and Carpenter and Homsy [3]. Our results coincide within a small difference with those given by Carpenter and Homsy [3]. For $Pr = 1$ and $Re = 10^4$ they obtain, e.g. $u(x = 0.5, y = 1) = 2.96 \times 10^{-2}$, which differs from our result (3.1×10^{-2}) only by -3%. The same comparison at $Pr = 10$ and $Re = 10^3$ yields a difference of 2%. We consider this favorable comparison as a proof of the correctness of our code and interpret the magnitude of the difference between both results as an error estimate.

4.2. *The structure of the main vortex: a comparison between 2D and 3D results*

Given that the 2D solution on the 32×32 grid has nearly converged to the 'exact' solution one can expect a 3D MG solution on a 32^3-grid to have a comparable accuracy. Therefore, for all subsequent 3D calculations we have used a three-level MG algorithm with grid sizes 8^3, 16^3 and 32^3. For all parameters considered the solution has proven to be symmetric with respect to the plane $z = 0.5$, even when using asymmetrically disturbed initial values. We conclude that no symmetry breaking is present as, for instance, in short Taylor–Couette annuli, see Barten *et al.* [15].

A quantitative comparison between the 3D 32^3-solution and the corresponding 2D 256^2-solution for u and T at $x = z = 0.5$, $y = 1$ and the minimum value of v along $y = z = 0.5$ is made in Table 1. In the 2D case the differences between the values for u and v_{min} obtained on the 32^2 and the 256^2 grid (given in parentheses) are of O(2%), whereas the differences between the respective temperature fields are of O(5%). These deviations giving the magnitude of the numerical error are not uniform. Since the differences between the 2D and 3D calculations on the 32^2 and the 32^3 grid are of the same order of magnitude, the influence of the sidewalls on u and T at the selected location $x = 0.5$ cannot be reliably determined. Their influence on v_{min} on the other hand is stronger. v_{min} (3D) is up to 15% smaller than v_{min} (2D), which clearly shows the expected retarding action of the sidewalls in the fluid bulk. This damping effect is demonstrated in Fig. 2, where isotherms of the 3D solution are shown in cross-sections at $z = 0.1$ (a) and $z = 0.5$ (b).

It is observed in qualitative agreement with Babu and Korpella [8] that the surface velocity u at $x = 0.5$ is unexpectedly increased and that the surface temperature T is decreased in the 3D case as compared to the 2D one for $Ma = 100$ (Table 1). This Marangoni number is just in a range where convection is important but boundary layers have not yet developed. The convective effect generally leads to a reduced magnitude of the driving temperature gradient over those parts of the free surface ($0 < x < 0.5$) over which the fluid is accelerated towards the cold boundary. This is illustrated in Fig. 3, where the surface temperature is shown at $z = 0.5$ for $Pr = 1$ and different Reynolds numbers. The qualitative behavior is the same as for the 2D case [6]. The presence of sidewalls on the temperature field reduces this effect and as a result the magnitude of the temperature gradient in the acceleration region will be closer to that of the conducting

Table 1. Velocity u and temperature T on the free surface at $x = z = 0.5$, $y = 1$ and the minimum vertical velocity v_{min} taken along $y = z = 0.5$

	$u \times 10^2$		T		$v_{min} \times 10^2$	
Re	2D	3D	2D	3D	2D	3D
10	13.72	13.37	0.519	0.513	−2.26	−1.99
	(14.00)		(0.530)		(−2.31)	
100	11.05	11.12	0.632	0.620	−2.03	−1.82
	(11.00)		(0.655)		(−2.04)	
1000	5.20	5.10	0.659	0.655	−1.04	−0.91
	(5.12)		(0.688)		(−1.02)	
5000	3.88	3.57	0.564	0.587	−1.18	−1.01
	(3.82)		(0.598)		(−1.20)	
10 000	3.15	3.01	0.576	0.567	−1.19	−1.00
	(3.08)		(0.586)		(−1.19)	
50 000	1.92	1.76	0.599	0.590	−0.84	−0.75
	(1.85)		(0.553)		(−0.90)	

Values are given for 2D (32^2) and 3D (32^3) steady flow for different Reynolds numbers Re and $Pr = 1$. The more accurate values obtained on the 256×256 grid are given in parentheses.

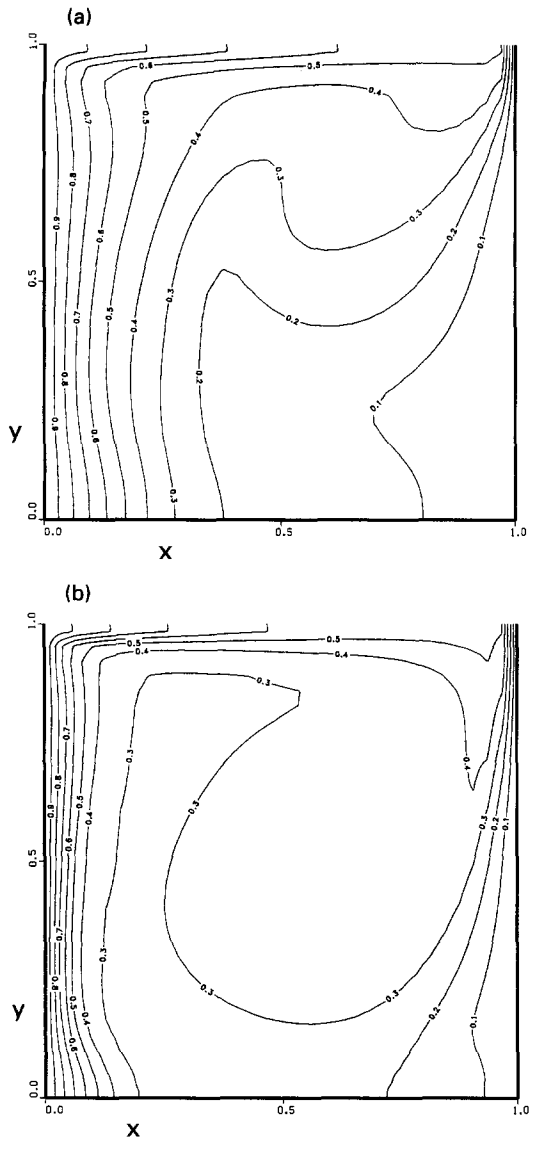

Fig. 2. Isotherms of the 3D solution for $Pr = 1$ and $Re = 5 \times 10^4$ at $z = 0.1$ (a) and $z = 0.5$ (b).

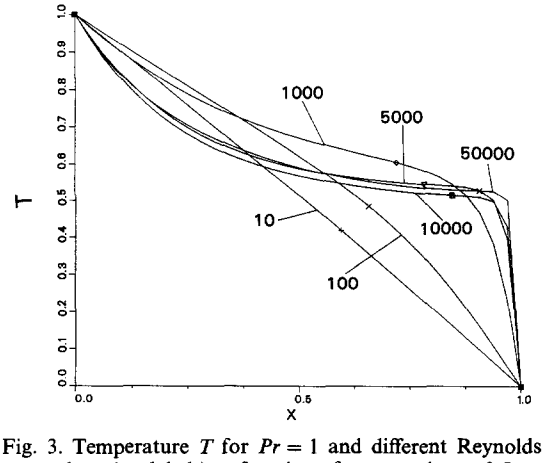

Fig. 3. Temperature T for $Pr = 1$ and different Reynolds numbers (see labels) as function of x at $y = 1$, $z = 0.5$.

profile leading to an enhanced surface flow in the 3D case.

The temperature close to the cold corner at $x = y = 1$ cannot be completely resolved with the present 32^3 grid due to the convective crowding of isotherms (cf. Fig. 2). Even though both the hot and the cold corner are singular [6], the isotherms in the bulk are reliably calculated, which we proved by comparing the solutions obtained on the 256^2 and the 32^2 grids of the 2D calculations. The isotherms indicate that the circulation in the x–y plane is getting weaker as the sidewalls $z = 0,1$ are approached. Note that the thickness of the thermal boundary layers at $x = 0$ and $x = 1$ increases towards these sidewalls. This will be important to the understanding of the secondary flow.

4.3. *Secondary vortices*

In the 3D thermocapillary driven cavity flow there appear a number of secondary vortices which are driven by different mechanisms. An overview of the main vortical structures is given in Fig. 4. The main or primary vortex (I) is by far the strongest one and has been discussed above. Vortices (II) and (III) are the well-known corner vortices, which arise due to flow separation in the presence of sharp rigid corners at $x = 0$, 1 and $y = 0$, cf. Moffatt [16]. As the vortex (I) develops for increasing Re to an inviscid core flow with approximately constant vorticity, these corner eddies can grow due to adverse pressure gradients along the vertical walls (Carpenter and Homsy [3]). They also appear in 2D thermocapillary flow [17], lid-driven cavity flow [18], and shear driven cavity flow [19]. As an example we show in Fig. 5 the velocity vectors projected onto the plane $z = 0.5$ for $Pr = 1$, $Re = 5 \times 10^4$. The size of the corner vortices is much smaller in the 3D than in the 2D flow, as a result of the retarding influence of the side walls.

Vortex (VI) and its symmetrically located counterpart have a thermocapillary origin. Since the velocity u vanishes when the vertical walls at $z = 0$, 1 are approached, the convective transport in x-direction at the free surface is reduced near $z = 0$, as compared to the midplane at $z = 0.5$. For small Marangoni number, however, convection leads to an increased slope $\partial_x T < 0$ at $x = 0$ as compared to $Ma = 0$ (creeping flow). Therefore, the gradient $\partial_x T(x = 0)$ is smaller close to the sidewalls at $z = 0$, 1 as compared to midplane $z = 0.5$ (for the absolute values we have $|\partial_x T(x \approx 0, y = 1, z \approx 0)| > |\partial_x T(x \approx 0, y = 1, z = 0.5)|$). This leads to a surface temperature distribution like that shown in Fig. 6(a). As a result thermocapillary forces directed toward the sidewalls are induced in z-direction and lead to well developed secondary vortices as shown in Fig. 7 (two upper vortices) in a cross-section at $x = 0.5$ for $Pr = 1$ and $Re = 100$. Profiles of the corresponding surface temperature and secondary surface velocity w at $x = 0.5$ are shown in Figs. 8(a) and 9(a) for $Ma = 100$ and four different Prandtl numbers. In the limit $Pr \to \infty$ with constant Ma equations (1–3) become inde-

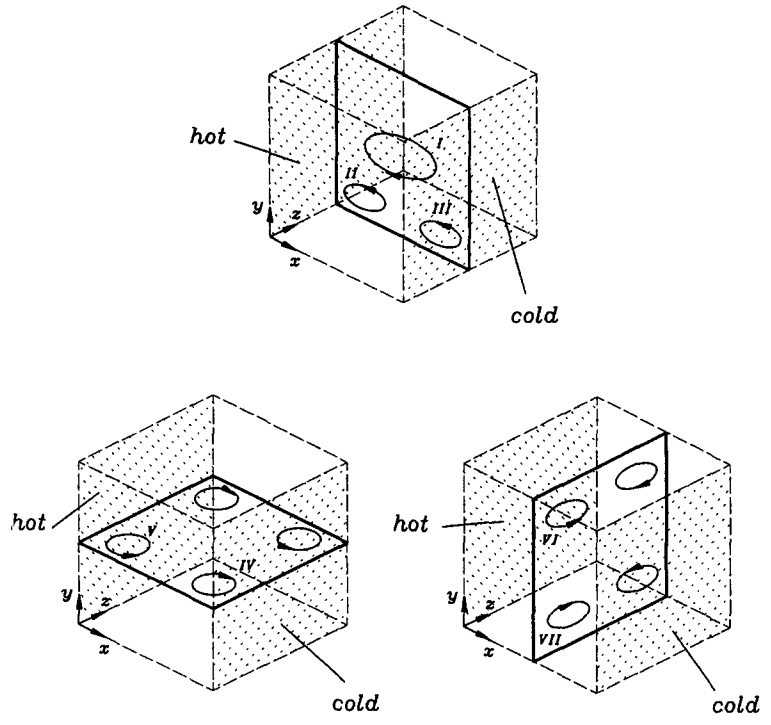

Fig. 4. Schematic representation of the primary and secondary vortical structures shown in the three orthogonal coordinate planes. The roman numbers are refered to in the text.

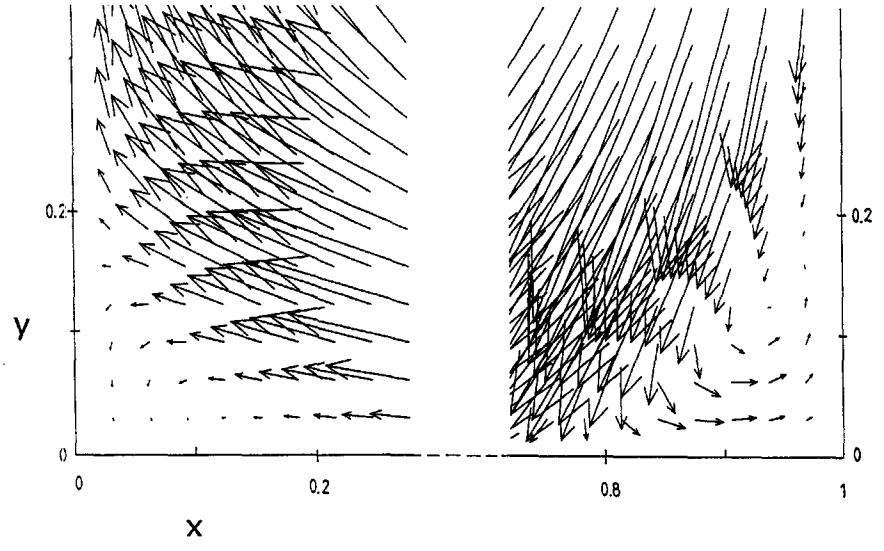

Fig. 5. Secondary vortices in the lower left and right corners in the plane $z = 0.5$, $x = 0$, 1 and $y = 0$ for 3D flow. All arrows are scaled identically.

pendent of *Re* and the solution is determined by *Ma* alone. It is seem from Figs. 8(a) and 9(a) that this asymptotic regime is reached for $Re < 10$ ($\triangleq Pr > 10$ at $Ma = 100$).

At high Marangoni numbers thermal boundary layers develop at $x = 0$ and $x = 1$. The appearance of the layer at $x = 0$ ($\partial_x T(x = 0)$ is now decreasing for increasing *Ma*) has the opposite effect on the free surface temperature distribution as compared to the small *Ma* number case. While close to the sidewalls the small *Ma* number effect dominates ($u \to 0$) shifting the free surface isotherms in positive x-direction downstream as z increases from 0 (z decreases from 1), the isotherms at $z = 0.5$ are compressed towards the cold ($x = 1$) *and* the hot boundary ($x = 0$). This results in a temperature distribution over the free surface, a typical example of which is shown in Fig. 6(b). The resulting surface forces in the z-direction

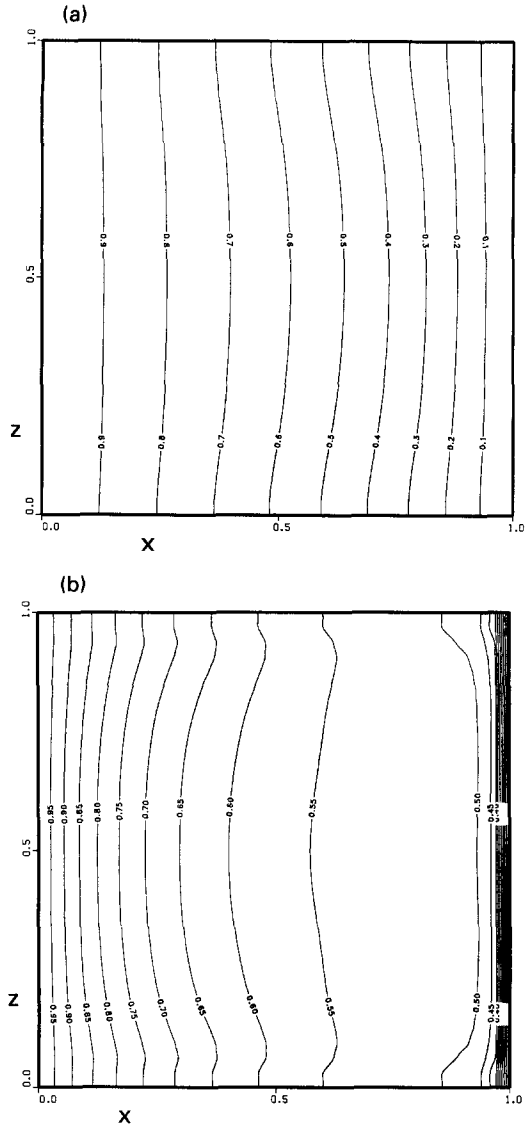

Fig. 6. Typical isotherms on the free surface ($y = 1$) for $Pr = 1$, small Marangoni number $Ma = 100$ (a) and large Marangoni number $Ma = 10^4$ (b).

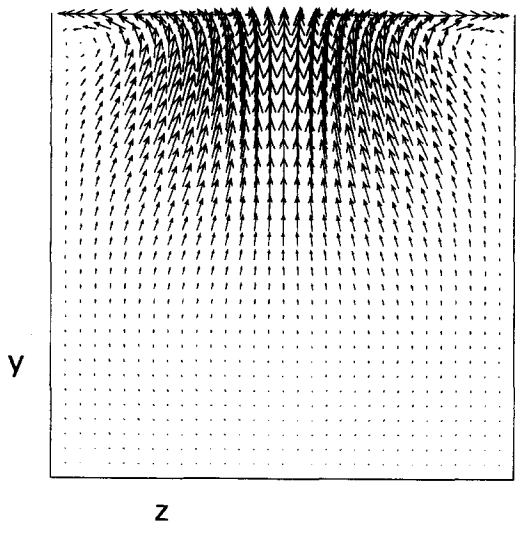

Fig. 7. Projection of velocity vectors onto the plane $x = 0.5$ for $Pr = 1$ and $Re = 100$.

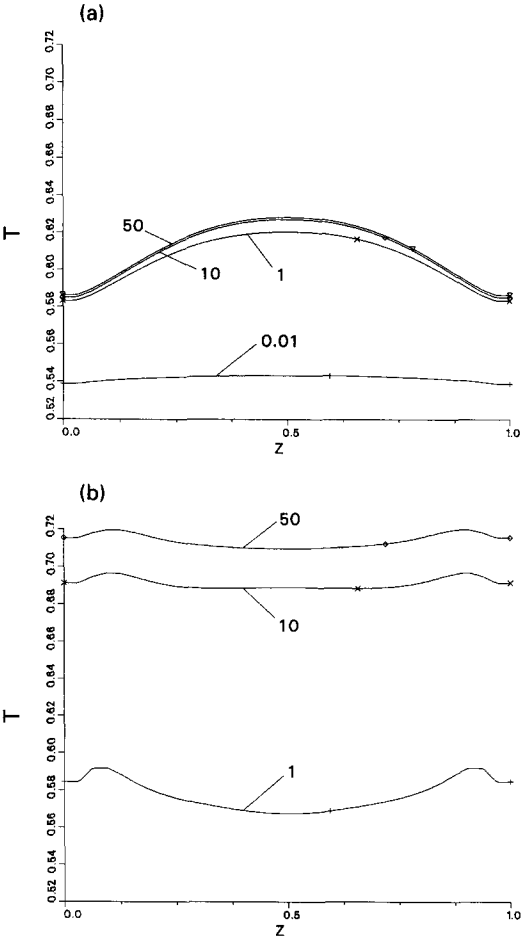

Fig. 8. Surface temperature T at $x = 0.5$ for $Ma = 100$ (a) and $Ma = 10^4$ (b) for different Pr as indicated by labels.

are always directed toward the insulating sidewalls in direct vicinity of the sidewalls. In an intermediate distance these forces are directed towards the wall near the cold side ($x = 1$) but opposite, i.e. towards the interior, near the hot side ($x = 0$). This mechanism induces secondary vortices close to free surface that have to compete, however, with other secondary vortices induced by the bulk fluid motion (see further below), which have a surface flow that is always directed towards the sidewalls. This competition is illustrated in Figs. 7 and 10 for $Pr = 1$ by showing cuts at $x = 0.5$. At small Re (Fig. 7) two secondary vortices are present due to the thermocapillary effect corresponding to Fig. 6(a). At increased Re and Ma the surface flow is directed towards the sidewalls in the vicinity of them while the surface flow is directed toward the center near $z = 0.5$ until, for higher Marangoni numbers (Fig. 10), the surface flow is directed towards the middle $z = 0.5$ nearly everywhere on the free surface except for a diminishing corner area. The

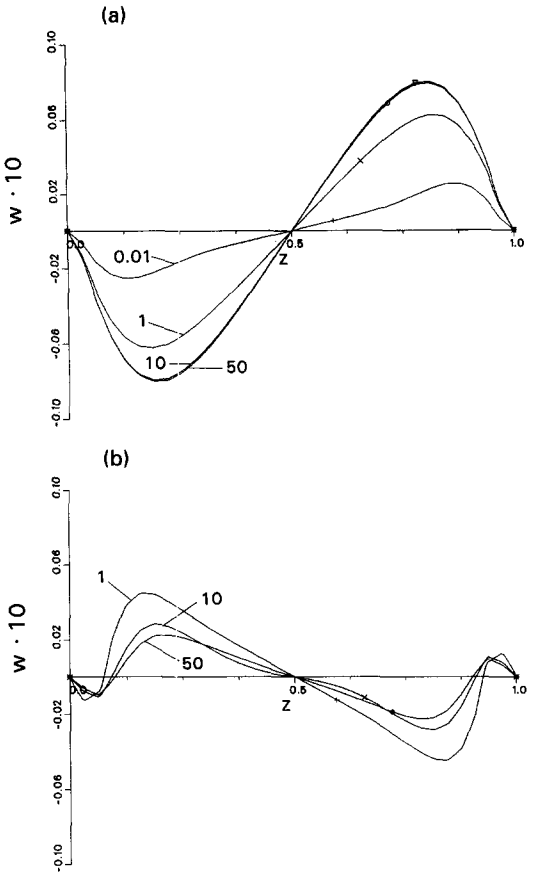

Fig. 9. Surface velocity w at $x = 0.5$ for $Ma = 100$ (a) and $Ma = 10^4$ (b) for different Pr as indicated by labels.

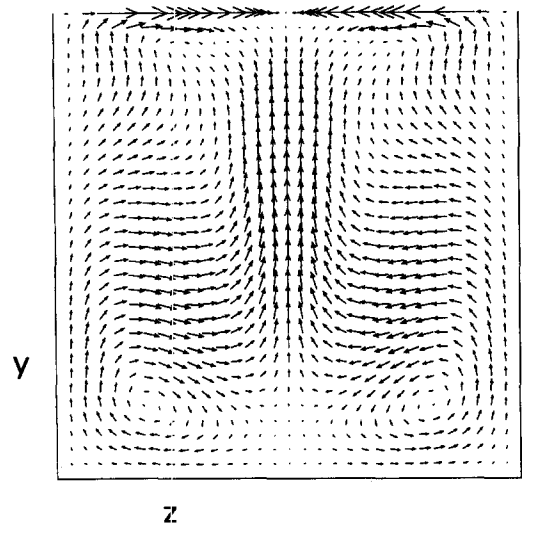

Fig. 10. Projection of the velocity vectors onto the plane $x = 0.5$ for $Pr = 1$ and $Re = 50\,000$.

fact that no visible vortices develop can be explained by counter-rotating vortices induced by the bulk motion (see further below). In Fig. 10 the competing forces get stronger and the thermocapillary induced vortex (clockwise in the upper left) close to the surface tends to separate from the counter-rotating bulk vortex (anti-clockwise in the middle left). Both vortices, however, are masked by the mean upflow in the upper half of the cavity at $x = 0.5$. Typical high Marangoni number profiles of T and w at $x = 0.5$ and $y = 1$ for $Ma = 10^4$ are shown in Figs. 8(b) and 9(b). They differ from Figs. 8(a) and 9(a) in that the asymptotic regime is not yet reached for $Pr = 50$ ($\triangleq Re = 200$).

The magnitude of the thermocapillary induced secondary flows (VI) relative to the main vortex flow (I) tends to zero as $Ma \to 0$. However, it gets larger as Ma increases and reaches the order of magnitude of 25% at $Pr = 1$ and $Re = 5 \times 10^4$. It should be mentioned that the above mechanism should also hold for the case of partially or even totally conducting sidewalls. As the thermal side wall conductance gets larger, we expect a strongly enhanced surface flow towards the sidewalls, since the temperature gradients in z-direction will necessarily be larger if the temperature on the sidewalls is forced to equal the conducting profile.

We now turn to the secondary vortices (VII) that are produced by the main vortex (I) in the vicinity of the sidewalls. For high Reynolds number the main vortex (I) develops to a rigidly rotating core flow with nearly constant vorticity [6]. Such flows induce Ekman boundary layers (Greenspan [20]) on the sidewalls at $z = 0,1$. Although this asymptotic parameter range has not yet been reached by the present investigation, the formation of secondary vortices near the boundaries at $z = 0,1$ is observed for increasing Reynolds (not Marangoni!) number. These are identified as Ekman vortices. The flow within the corresponding sidewall boundary layers is directed towards the axis of the main vortex, since the sidewalls are stationary. Here we observe the formation of one Ekman [21] or Bödewaldt [22, 23] vortex (VII) on each sidewall as the Reynolds number is increased. These vortices transport fluid from the sidewall Ekman layers, which are still comparatively thick, to the center of the cavity. The corresponding vortices (VII) are clearly visible in the bottom half of Fig. 10. A corresponding pair of Ekman vortices can also be expected near the free surface. However, thermocapillary forces on the free surface at $x = 0.5$ drive a motion opposite to the sense of rotation of the expected Ekman vortex if the Marangoni number is large and, as a consequence, a distinct Ekman vortex cannot be seen there. The secondary vortices (VII) at the bottom of the cavity extend in a curved fashion along the sidewalls up the hot and the cold boundaries. In Fig. 11 we show these vortices (IV, V) in horizontal cuts at $y = 0.625$. In the x–z plane the centers of the vortices (IV) at the cold side ($x = 1$) are located very close to the corners near the free surface ($y \approx 1$), while they are found in the interior near $z = 0.5$ close to the bottom ($y \approx 0$). The vortices (V) on the hot side ($x = 0$) show the opposite behavior. This effect is due to the main vortex (I) which is responsible for a strong flow in positive x-

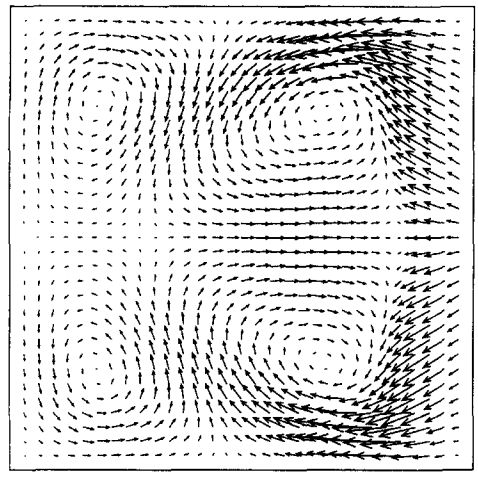

Fig. 11. Vortical structures in the plane $y = 0.625$ for $Pr = 1$ and $Re = 5 \times 10^4$.

direction in the upper part of the cavity and for a flow in negative x-direction in the lower part of it. This main flow is superposed to the Ekman vortices (IV, V, VII) seemingly shifting them toward or away from the heated walls depending on the sign of u.

5. CONCLUSIONS

The steady 3D thermocapillary flow in an open cubic cavity has successfully been calculated up to Marangoni numbers as large as $Ma = 5 \times 10^4$. The employed FAS–FMG algorithm has proven to be an efficient method for this purpose. A typical calculation took about 4 h on an IBM RS 6000/530 series workstation. A mesh of 32^3-grid points turned out to have an accuracy better than 5% (except for the peak velocities near the cold corner) and thus being capable of reliably compute secondary flow structures due to the presence of sidewalls. These secondary flows have been explained in terms of (a) additional thermocapillary actions perpendicular to the main thermocapillary driving force and (b) Ekman vortices on the sidewalls. Close to the free surface and depending on the x-position, Pr and Re number, both vortices can reinforce or annihilate each other. It was found that the secondary thermocapillary flows appeared due to an increase of the Marangoni number, whereas the Ekman vortices being independent of the temperature field appear due to increasing Reynolds number. Within the range of parameters investigated we have not found any Taylor–Görtler like vortices [24].

Though steady high Marangoni number flow has been considered we have not investigated its stability to time-dependent perturbations. It is well known that time-dependence can set in even in 2D driven cavity flow (see for instance Goodrich *et al.* [25]). Little is known, however, about the onset of time-dependence in thermocapillary cavities and about the possibly stabilizing influence of sidewalls. This question will be an interesting research subject for future investigations.

Acknowledgements—The authors acknowledge the support of the Deutsche Agentur für Raumfahrtangelegenheiten (DARA) under grant number 50-QV 88981.

REFERENCES

1. W. H. Gieldt, Welding—An interdisciplinary science and technology. In *Interdisciplinary Issues in Materials Processing Manufacturing* (Edited by S. K. Samanta, R. Komanduri, R. McMeeking, M. M. Chen and A. Tseng). ASME, New York (1987).
2. M. Mihelčić and K. Wingerath, Three-dimensional simulations of the Czochralski bulk flow in a stationary transverse field and a vertical magnetic field: effects on the asymmetry of the flow and temperature distribution in the Si melt, *J. Crystal Growth* **82,** 318 (1987).
3. B. M. Carpenter and G. M. Homsy, High Marangoni convection in a square cavity—II, *Phys. Fluids A* **2**(2), 137 (1990).
4. G. Graziani, M. Strani and R. Piva, Effect of free surface radiation in asymmetric thermocapillary flow, *Acta Astronautica* **9**(4), 231 (1982).
5. M. Strani, R. Piva and G. Graziani, Thermocapillary convection in a rectangular cavity: asymptotic theory and numerical simulation, *J. Fluid Mech.* **130,** 347 (1983).
6. A. Zebib, G. M. Homsy and E. Meiburg, High Marangoni convection in a square cavity, *Phys. Fluids* **28**(12), 3467 (1985).
7. U. Ghia, K. N. Ghia and C. T. Shin, High-Re solutions for incompressible flow using the Navier–Stokes equations and a multigrid method *J. Comp. Phys.* **48,** 387 (1982).
8. V. Babu and S. A. Korpela, Three-dimensional thermocapillary convection in a cavity, *Computers Fluids* **18**(2), 229 (1990).
9. K. C. Hsieh, A numerical study of three-dimensional surface tension driven convection with free surface deformation, *Fluid Mechanics Phenomena in Microgravity* ASME-AMD-Vol. 154/FED-Vol. 142, 85 (1992).
10. Y. Kamotani, S. Ostrach and M. Vargas, *J. Crystal Growth* **66,** 83 (1984).
11. C. H. Bruneau and C. Jouron, An efficient scheme for solving steady incompressible Navier–Stokes equations, *J. Comp. Phys.* **89,** 389 (1990).
12. S. P. Vanka, Block implicit multi-grid solution of Navier–Stokes equations in primitive variables, *J. Comp. Phys.* **65,** 138 (1986).
13. D. B. Spalding, A novel finite difference formulation for differential expressions involving both first and second derivatives, *Int. J. Numer. Meth. Engng* **4,** 551 (1972).
14. M. C. Thompson and J. H. Ferzinger, An adaptive multigrid technique for the incompressible Navier–Stokes equations, *J. Comp. Phys.* **82,** 94 (1989).
15. W. Barten, M. Lücke and M. Kamps, Conservation and breaking of mirror symmetry in a numerical simulation of vortex flow, *J. Comp. Phys.* **91,** 486 (1990).
16. H. K. Moffatt, Viscous and resistive eddies near a sharp corner, *J. Fluid Mech.* **18,** 1 (1963).
17. V. Saß, A. Delgado and H. J. Rath, Numerische Simulation der Marangonikonvektion in einem offenen Boot mit einem Multi-Grid-Verfahren, *Z. Angew. Math. Mech.* **72**(6), T529 (1992).
18. R. Schreiber and H. B. Keller, Driven cavity flows by efficient numerical techniques, *J. Comp. Phys.* **49,** 310 (1983).
19. N. K. Ghaddar, K. Z. Korczak, B. B. Mikic and A. T.

Patera, Numerical investigation of incompressible flow in grooved channels—I. Stability and self-sustained oscillations, *J. Fluid Mech.* **163,** 99 (1986).
20. H. P. Greenspan, *The Theory of Rotating Fluids.* Cambridge University Press, Cambridge U.K. (1968).
21. V. W. Ekman, On the influence of earth's rotation on ocean-currents, *Ark. Mat. Astr. Fys.* **2,** 1 (1905).
22. U. T. Bödewaldt, Die Drehströmung über festem Grunde, *Z. Angew. Math. Mech.* **20,** 241 (1940).
23. S. H. Davis, Convection in a box, *J. Fluid Mech.* **30,** 465 (1967).
24. M. Deville, T.-H. Lê and Y. Morchoisne (Eds), Numerical simulation of 3-D incompressible unsteady viscous laminar flows. In *Notes on Numerical Fluid Mechanics,* Vol. 36. Vieweg, Braunschweig (1992).
25. J. W. Goodrich, K. Gustafson and K. Halasi, Hopf bifurcation in the driven cavity, *J. Comp. Phys.* **90,** 219 (1990).